

# An adaptive meshfree Galerkin method for the three-dimensional thermo-mechanical flow simulation of friction stir welding process

W. Hu<sup>1</sup>, C.T. Wu<sup>1</sup>, H.P. Wang<sup>2</sup> and H. Lu<sup>3</sup>

*Affiliations*

<sup>1</sup> Livermore Software Technology Corporation, 7374 Las Positas Road, Livermore, CA 94551

<sup>2</sup> GM Research and Development Center, 30500 Mound Road, Warren, MI 48090-9055, USA

<sup>3</sup> Hengstar Technology Co. Ltd., Room 11206, 11 Guoshoujing Rd., Shanghai, 201203, China

## Abstract

*In this paper, new numerical modeling of material flow in the thermo-mechanical friction stir welding process is presented. In this numerical model, the discretization in space is derived by the meshfree Galerkin method using a Lagrangian meshfree convex approximation. The discrete thermal and mechanical equations are weakly coupled as the time advances using a forward difference scheme. A mortar contact algorithm is employed to model the stirring effect and heat generation due to frictional contact. Heat conductance between contacting bodies is considered as a function of contact pressure. A two-way adaptive procedure is introduced to the coupled thermo-mechanical system to surpass potential numerical problems associated with the extensive material deformation and spatial discretization. In each adaptive phase, a consistent projection operation utilizing the first-order meshfree convex approximation is performed to remap the solution variables. Finally, a three-dimensional thermo-mechanical coupled friction stir welding problem is analyzed to demonstrate the effectiveness of the present formulation.*

**Keywords:** Friction stir welding, finite element, meshfree, adaptive

## 1. Introduction

Friction stir welding (FSW) is an innovative welding method [Dawes 1996] that is viable for jointing aluminum alloys, copper, magnesium and other low-melting point metallic materials. It combines frictional heating and stirring motion to soften and mix the interface between two work pieces yielding to a solid and fully consolidated weld. Since FWS is a solid state jointing process, a high quality weld can be achieved with the absence of solidification cracking, porosity, oxidation and other defects typical to traditional fusion welding. FSW offers high levels of repeatability, limited energy consumption and ease of automation, and thus gains its popularity in aerospace, automotive, railway and nuclear industries. The FSW process consists of four basic phases namely, the plunging, stirring, welding and retraction. The plunging phase starts with plunging the rigid cylindrical spinning tool into the joint line until the shoulder contacts the top surface of work piece. In stirring phase, the heat is generated by means of work from frictional contact and material plastic deformation. This heat is dissipated into the welding zone and results in an increase of temperature and material softening. In particular, the heat generated from frictional contact plays an important role in determining the material rheological behavior and

the success of the deposition welding process. The welding phase is initiated by moving either the tool or the work piece and enables the materials of two work pieces to mix together. Finally, the welding process stops and the tool retract from the work piece. These four FSW phases constitute complicated thermo-mechanical conditions which are very hard to determine experimentally [Lorrain 2009]. Despite many successful experimental investigations have already been conducted to the adjustment of tool profile and input weld parameters such as tool speed, feed rate and tool depth, several aspects of the FSW are still poorly understood and require further study [Neto 2013]. In particular, understanding the temperature distributions in the work piece during FSW process is an essential subject [Pashazadeh 2013] due to its effects on the material flow, grain size, residual stresses and subsequently, the strength.

It is recognized that a correct numerical model of the FSW process should avoid any unnecessary assumptions. A list of requirements [Neto 2013] for FSW analysis code should include (1) Rotational boundary condition; (2) Frictional contact algorithm; (3) Support for very high levels of deformation; (4) Elastic-plastic or elastic-viscoplastic material models; and (5) Support for complex geometry. The main difficulty in finite element modeling of FSW process consists in dealing with high levels of deformations involving in the complex material flow due to frictional heating and stirring motion. The numerical complexity in Eulerian formulation is concerning the needs to model free surface, the welding heat source, and material histories. An alternative approach is the use of adaptive meshfree method [Lu 2006, Lu 2008, Wu 2009, Wang 2009, Hu 2010]. The objective of this study is to present a meshfree Galerkin approach [Wu 2014] using the Lagrangian meshfree convex approximation [Wu 2011] and a two-way adaptive procedure for the simulation of FSW process. The reminder of the paper is organized as follows: The coupled thermo-mechanical equations in FSW problem and their numerical model using Lagrangian meshfree convex approximations are given in Section 2. The computational strategies for the two-way adaptive procedure and the remap algorithm are given in Section 3. Finally, a numerical example is presented in Section 4.

## 2. Governing Equation

### 2.1. Thermal Problem

We consider the transient heat transfer response of a FSW work piece in a three-dimension case. We assume the domain of the work piece  $\Omega \subset \mathcal{R}^3$  is a bounded polygon with disjointed boundary  $\partial\Omega = \partial\Omega_d \cup \partial\Omega_n \cup \partial\Omega_c \cup \partial\Omega_{cr}$ . The notation  $\partial\Omega_d$  describes a Dirichlet boundary imposed by a temperature  $\theta$ .  $\partial\Omega_n$  is the Neumann boundary prescribed by a heat flux. We also assume that  $\partial\Omega_d$  and  $\partial\Omega_n$  do not vary with time. The boundary  $\partial\Omega_c$  denotes the contact surface with a thermal exchange due the conduction between the tool and work piece. The boundary  $\partial\Omega_{cr}$  is the surface with the thermal exchange due to convection and radiation. We further assume the heat generation in the work piece is only due to the plastic deformation and frictional contact between tool and work piece. Giving an internal heat generation rate  $Q$  per unit deformed volume from the plastic deformation, the strong form of the thermal energy conservation equation reads

$$\rho C_p \dot{\theta} + \nabla \cdot \mathbf{q} = Q \quad \text{in } \Omega \times ]0, T[ \quad (1)$$

$$\mathbf{q} := -k(\nabla\theta) \quad (2)$$

$$Q := \eta \mathbf{S} : \dot{\boldsymbol{\varepsilon}}^p \quad (3)$$

subject to boundary conditions

$$\theta = \theta_d \quad \text{on } \partial\Omega_d \times ]0, T[ \quad (4)$$

$$-\mathbf{q} \cdot \mathbf{n} = q_n \quad \text{on } \partial\Omega_n \times ]0, T[ \quad (5)$$

$$-\mathbf{q} \cdot \mathbf{n} = h_{cd}(\theta - \theta_{tool}) + \beta \boldsymbol{\lambda} \cdot [\dot{\mathbf{u}}^t] \quad \text{on } \partial\Omega_c \times ]0, T[ \quad (6)$$

$$-\mathbf{q} \cdot \mathbf{n} = h_{cv}(\theta - \theta_a) + h_r(\theta - \theta_a) \quad \text{on } \partial\Omega_{cr} \times ]0, T[ \quad (7)$$

and initial condition at time  $t=0$

$$\theta(\mathbf{X}, 0) = \theta_0(\mathbf{X}) \quad \text{in } \Omega \quad (8)$$

where  $\rho$  is the mass density and  $C_p$  is the heat capacity. Eq. (2) is known as the Fourier law [Hughes 2000] with  $k$  denoting the isotropic thermal conductivity.  $\nabla$  is the gradient operator with respect to current position  $\mathbf{x}$  and “ $\nabla \cdot$ ” denotes the divergence operator. The Taylor-Quinney [Marusich 1995] coefficient  $\eta$  in Eq. (3) takes into account the fraction of heat generated by the plastic deformation energy dissipation.  $\mathbf{S}$  and  $\dot{\boldsymbol{\varepsilon}}^p$  are the deviatoric part of Cauchy stress and the rate of plastic straining, respectively.  $\theta_d$  in Eq. (4) is the temperature imposed on the Dirichlet boundary.  $q_n$  in Eq. (5) is the normal heat flux imposed on the Neumann boundary.  $h_{cd}$ ,  $h_{cv}$  and  $h_r$  are heat transfer coefficients for conduction, convection and radiation, respectively. The notation  $\mathbf{n}$  defines the outward unit normal vector on  $\partial\Omega$ . The second term on the right-hand side of Eq. (6) represents the rate of frictional energy dissipation where  $\beta$  is the fraction of heat generated by the frictional contact.  $\boldsymbol{\lambda}$  is the Cauchy contact traction and  $[\dot{\mathbf{u}}^t]$  is the contact slip rate which represents the jump in velocity across the contact.  $\theta_a$  is the ambient temperature and  $\theta_{tool}$  is the temperature of the tool.  $\mathbf{X}$  in Eq. (8) is the position vector in the reference configuration. It is also necessary to match the initial condition with the Dirichlet boundary condition at time  $t=0$ :

$$\theta_0(\mathbf{X}) = \theta_d(\mathbf{X}, 0) \quad \text{on } \partial\Omega_d \quad (9)$$

The variational formulation of the thermal energy conservation equation can be written to find the temperature field  $\theta(\mathbf{X}, t) \in \Theta = \{\theta \in H^1(\Omega) : \theta = \theta_d \text{ on } \partial\Omega_d\}$  such that for arbitrary variation  $\delta\theta \in \Theta_0 = \{\theta \in H^1(\Omega) : \theta = 0 \text{ on } \partial\Omega_d\}$  the following equation is satisfied

$$\begin{aligned} \int_{\Omega} \rho C_p \dot{\theta} \delta\theta d\Omega + \int_{\Omega} k \nabla \theta \cdot \nabla(\delta\theta) d\Omega = \int_{\Omega} Q \delta\theta d\Omega + \int_{\partial\Omega_n} q_n \delta\theta ds \\ + \int_{\partial\Omega_c} (h_{cd}(\theta - \theta_{tool}) + \beta \boldsymbol{\lambda} \cdot [\dot{\mathbf{u}}^t]) \delta\theta ds + \int_{\partial\Omega_{cr}} (h_{cv} + h_r)(\theta - \theta_a) \delta\theta ds \end{aligned} \quad (10)$$

## 2.2. Mechanical Problem

The motion of the FSW work piece is governed by the equation of motion with the prescribed boundary and initial conditions. The mechanical problem is given as follows:

$$\rho \ddot{\mathbf{u}} = \nabla \cdot \boldsymbol{\sigma} + \mathbf{b} \text{ in } \Omega \times ]0, T[ \quad (11)$$

subject to Dirichlet and Neumann boundary conditions

$$\mathbf{u} = \mathbf{u}_g \text{ on } \partial\Omega_g \times ]0, T[ \quad (12)$$

$$\boldsymbol{\sigma} \cdot \mathbf{n} = \mathbf{h} \text{ on } \partial\Omega_h \times ]0, T[ \quad (13)$$

together with unilateral contact conditions

$$\begin{cases} g \leq 0 \\ -\boldsymbol{\lambda} \cdot \mathbf{n}^c = \lambda^n \geq 0 \text{ on } \partial\Omega_c \times ]0, T[ \\ \lambda^n g = 0 \end{cases} \quad (14)$$

and Coulomb friction conditions

$$\begin{cases} \text{if } \|\boldsymbol{\lambda}'\| < \mu(\theta) \|\lambda^n\| \text{ then } [\dot{\mathbf{u}}^t] = \mathbf{0} \\ \text{if } \|\boldsymbol{\lambda}'\| = \mu(\theta) \|\lambda^n\| \text{ then } \exists \omega \geq 0 : [\dot{\mathbf{u}}^t] = \omega \boldsymbol{\lambda}' \end{cases} \text{ on } \partial\Omega_c \times ]0, T[ \quad (15)$$

and initial conditions

$$\mathbf{u}(\mathbf{X}, 0) = \mathbf{u}_0(\mathbf{X}) \quad (16)$$

$$\dot{\mathbf{u}}(\mathbf{X}, 0) = \dot{\mathbf{u}}_0(\mathbf{X}) \quad (17)$$

where  $\mathbf{b}$  is the body force vector and  $\boldsymbol{\sigma}$  is the Cauchy stress obtained from the constitutive law. The notation  $\partial\Omega_g$  describes a Dirichlet boundary imposed by a displacement  $\mathbf{u}_g$  and  $\partial\Omega_h$  is the Neumann boundary prescribed by a surface traction  $\mathbf{h}$  with  $\partial\Omega_g \cap \partial\Omega_h = \emptyset$ . The notation  $g$  in Eq. (14) is the contact gap function.  $\mathbf{n}^c$  denotes the outward unit normal to contact surface  $\partial\Omega_c$ .  $\boldsymbol{\lambda}'$  is the tangential component of contact traction  $\boldsymbol{\lambda}$ . Eq. (15) states that the vector of slip rate  $[\dot{\mathbf{u}}^t]$  should be in the direction of tangential traction.  $\mu(\theta)$  is the temperature dependent friction coefficient.  $\|\cdot\|$  stands for the Euclidean norm.  $\mathbf{u}_0$  and  $\dot{\mathbf{u}}_0$  are the initial displacement and velocity, respectively.

Subsequently, the variational equation for the mechanical problem in FSW process is formulated using the integration by part to find the displacement field  $\mathbf{u}(\mathbf{X}, t) \in \mathcal{V} = \{\mathbf{u} \in \mathbf{H}^1(\Omega) : \mathbf{u} = \mathbf{u}_g \text{ on } \partial\Omega_g\}$ , such that for arbitrary variation  $\delta\mathbf{u} \in \mathcal{V}_0 = \{\mathbf{u} \in \mathbf{H}^1(\Omega) : \mathbf{u} = \mathbf{0} \text{ on } \partial\Omega_g\}$ , the following equation is satisfied:

$$\int_{\Omega} \rho \ddot{\mathbf{u}} \cdot \delta\mathbf{u} d\Omega + \int_{\Omega} \boldsymbol{\sigma} : \nabla^s(\delta\mathbf{u}) d\Omega = \int_{\Omega} \mathbf{b} \cdot \delta\mathbf{u} d\Omega + \int_{\partial\Omega_h} \mathbf{h} \cdot \delta\mathbf{u} ds + \int_{\partial\Omega_c} \boldsymbol{\lambda} \cdot \delta\mathbf{u} ds \quad (18)$$

Now the FSW problem is stated by coupling the mechanical weak form in Eq. (18) with the thermal weak form in Eq. (10) and subjecting to the prescribed Dirichlet boundaries and initial conditions.

### 2.3 Thermo-mechanical Equations

The standard Galerkin method is formulated on a finite dimensional space  $\Theta^h \subset \Theta$  employing the thermal weak form of Eq. (10) to find  $\theta^h(t) \in \Theta^h$  such that

$$\begin{aligned} \int_{\Omega} \rho C_p \dot{\theta}^h \delta \theta^h d\Omega + \int_{\Omega} k \nabla \theta^h \cdot \nabla (\delta \theta^h) d\Omega = \int_{\Omega} Q \delta \theta^h d\Omega + \int_{\partial \Omega_{nT}} q_n \delta \theta^h ds \\ + \int_{\partial \Omega_c} (h_{cd} (\theta^h - \theta_{tool}) + \beta \lambda \cdot [\dot{\mathbf{u}}^t]) \delta \theta^h ds + \int_{\partial \Omega_{cr}} (h_{cv} + h_r) (\theta^h - \theta_a) \delta \theta^h ds \quad \forall \delta \theta^h \in \Theta_0^h \end{aligned} \quad (19)$$

with

$$\theta^h(\mathbf{X}, 0) = \theta_0(\mathbf{X}) \text{ in } \Omega \quad (20)$$

where  $\Theta^h = \text{span}\{\Psi_I : I \in Z_I\}$  and  $Z_I$  is an index set.  $\{\Psi_I\}_{I \in Z_I}$  are meshfree shape functions. Similarly, we have the mechanical weak form of Eq. (18) to find  $\mathbf{u}^h(\mathbf{X}, t) \in V^h$  such that

$$\int_{\Omega} \rho \ddot{\mathbf{u}}^h \cdot \delta \mathbf{u}^h d\Omega + \int_{\Omega} \boldsymbol{\sigma} : \nabla^s (\delta \mathbf{u}^h) d\Omega = \int_{\Omega} \mathbf{b} \cdot \delta \mathbf{u}^h d\Omega + \int_{\partial \Omega_n} \mathbf{h} \cdot \delta \mathbf{u}^h ds + \int_{\partial \Omega_c} \boldsymbol{\lambda} \cdot \delta \mathbf{u}^h ds \quad \forall \delta \mathbf{u}^h \in V_0^h \quad (21)$$

with initial conditions defined in Eqs. (16) and (17).

In Lagrangian formulation with meshfree discretization, discrete points that carry the primary unknown variables are attached to the same set of material points throughout the course of deformation. Under this consideration, the node set  $Z_I = \{\mathbf{X}_I, I = 1, \dots, NP\}$  is the set of nodes defined in the reference configuration. In practice, the set of meshfree nodes can be taken from the finite element nodes created by a finite element mesh generator. The material displacements and temperature fields are approximated using the Lagrangian meshfree shape functions [Chen 1996; Wu 2001] as

$$\mathbf{u}^h(\mathbf{X}, t) = \sum_{I=1}^{NP} \Psi_I(\mathbf{X}) \mathbf{u}(\mathbf{X}_I, t) = \sum_{I=1}^{NP} \Psi_I(\mathbf{X}) \tilde{\mathbf{u}}_I(t) \quad \forall \mathbf{X} \in \Omega_X \quad (22)$$

$$\theta^h(\mathbf{X}, t) = \sum_{I=1}^{NP} \Psi_I(\mathbf{X}) \tilde{\theta}_I(t) \quad \forall \mathbf{X} \in \Omega_X \quad (23)$$

where  $\tilde{\mathbf{u}}_I := \mathbf{u}(\mathbf{X}_I, t)$  and  $\tilde{\theta}_I(t) := \theta(\mathbf{X}_I, t)$  are called the ‘generalized’ displacement and temperature of node  $I$ . Conventional meshfree approximations are generally not interpolants, i.e.,  $\tilde{\mathbf{u}}_I(t) \neq \mathbf{u}^h(\mathbf{X}_I, t)$  and  $\tilde{\theta}_I(t) \neq \theta^h(\mathbf{X}_I, t)$ . In this study an alternative meshfree approximation that restores a weak Kronecker-delta property at the boundary, the meshfree convex approximation [Sukumar 2004; Arroy 2005; Wu 2011], is utilized to allow the direct treatment of Dirichlet boundary conditions for FSW problem. We employ the first-order convex GMF [Wu 2011] method to obtain the meshfree convex approximation using the inverse tangent basis function and the cubic spline weight function.

Substituting Eqs. (22) and (23) into Eqs. (21) and (19) using meshfree convex approximation, the semi-discrete equations of the coupled thermo-mechanical problem can be expressed by the following algebraic equations,

$$\mathbf{C}\ddot{\boldsymbol{\theta}} + \mathbf{H}\ddot{\boldsymbol{\theta}} = \mathbf{P} \quad (24)$$

$$\mathbf{M}\ddot{\mathbf{U}} = \mathbf{F}^{ext} + \mathbf{F}^c - \mathbf{F}^{int} \quad (25)$$

where

$$C_{IJ} = \int_{\Omega_X} \rho_0 C_p \Psi_I \Psi_J d\Omega_X \quad (26)$$

$$H_{IJ} = \int_{\Omega_X} k F_{il}^{-1} F_{lj}^{-T} \Psi_{I,l} \Psi_{J,i} J_0 d\Omega_X + \int_{\partial\Omega_c} h_{cd} \Psi_I \Psi_J ds + \int_{\partial\Omega_{cr}} (h_{cv} + h_r) \Psi_I \Psi_J ds \quad (27)$$

$$P_I = \int_{\Omega_X} \eta \mathbf{S} : \dot{\boldsymbol{\varepsilon}}^p J_0 \Psi_I d\Omega_X + \int_{\partial\Omega_n} q_n \Psi_I ds + \int_{\partial\Omega_c} (h_{cd} \theta_{tool} - \beta \boldsymbol{\lambda} \cdot [\dot{\mathbf{u}}^t]) \Psi_I ds + \int_{\partial\Omega_{cr}} (h_{cv} + h_r) \theta_a \Psi_I ds \quad (28)$$

$$\mathbf{M}_{IJ} = \int_{\Omega_X} \rho_0 \Psi_I \Psi_J \mathbf{I} d\Omega_X \quad (29)$$

$$\mathbf{F}_I^{ext} = \int_{\partial\Omega_h} \mathbf{h} \Psi_I ds + \int_{\Omega_X} \mathbf{b} \Psi_I J_0 d\Omega_X \quad (30)$$

$$\mathbf{F}_I^c = \int_{\partial\Omega_c} \boldsymbol{\lambda} \Psi_I ds \quad (31)$$

$$\mathbf{F}_I^{int} = \int_{\Omega_X} \boldsymbol{\sigma}_0 : \nabla_X \Psi_I d\Omega_X \quad (32)$$

$$\mathbf{F} = \nabla_X \mathbf{x} \quad (33)$$

$$J_0 = \det(\mathbf{F}) \quad (34)$$

$$\boldsymbol{\sigma}_0 = J_0 \boldsymbol{\sigma} \mathbf{F}^{-T} \quad (35)$$

$$\tilde{\boldsymbol{\theta}} = [\boldsymbol{\theta}^b, \tilde{\boldsymbol{\theta}}^i]^T \quad (36)$$

$$\tilde{\mathbf{U}} = [\mathbf{U}^b, \tilde{\mathbf{U}}^i]^T \quad (37)$$

$$\boldsymbol{\theta}^b = [\theta_1^b, \theta_2^b, \dots, \theta_{NB}^b], \tilde{\boldsymbol{\theta}}^i = [\tilde{\theta}_1^i, \tilde{\theta}_2^i, \dots, \tilde{\theta}_{NI}^i], NB + NI = NP \quad (38)$$

$$\mathbf{U}^b = [\mathbf{u}_1^b, \mathbf{u}_2^b, \dots, \mathbf{u}_{NB}^b], \tilde{\mathbf{U}}^i = [\tilde{\mathbf{u}}_1^i, \tilde{\mathbf{u}}_2^i, \dots, \tilde{\mathbf{u}}_{NI}^i] \quad (39)$$

where  $\mathbf{F}^c$  is contact force, and  $\boldsymbol{\lambda}$  is contact traction calculated using mortar contact algorithm [Puso and Laursen 2004, Yang *et al.* 2005];  $\nabla_X$  denotes the material gradient operator. For the implementation purpose, all terms associated with the volume integration are evaluated on the reference configuration and the surface integration terms are computed on the current configuration. Using Nanson's formula, the Cauchy stress appears in the internal force term is transformed to the first Piola-Kirchhoff stress tensor  $\boldsymbol{\sigma}_0$ . Note that we have used the chain rule  $\nabla \Psi_I = \mathbf{F}^{-T} \nabla_X \Psi_I$  for the spatial gradient operation in the above derivations.  $\tilde{\boldsymbol{\theta}}^i$  and  $\tilde{\mathbf{U}}^i$  are vectors of generalized nodal values for the interior nodes to be solved for the temperature and displacement fields, respectively. With the meshfree convex approximation, the unknown nodal vectors of temperature and displacement fields for boundary nodes are denoted by  $\boldsymbol{\theta}^b$  and  $\mathbf{U}^b$  respectively. For convenience, the finite element mesh is taken as the integration cells [Chen 1996; Wu 2001] for the domain integration. Each integration cell occupies an initial volume needed in the domain integration and the one-point integration rule is used for each integration cell in the computation. The integration cells also provide a set of boundary nodes information for the contact traction calculation as described in the next sub-section.

## 2.4 Time Discretization

The highly coupled and nonlinear system in the FSW thermo-mechanical equations are difficult to solve by simultaneous time-stepping algorithm. The large and un-symmetric system in the fully coupled thermo-mechanical equations inevitably involves the convergent problem and is expensive to solve, particularly in the presence of large deformation, severe contact conditions and contact-induced thermal shock. In the application of interest, explicit and staggered time-stepping schemes [Marusich 1995; Koric 2009] are considered in this study.

The thermal equation in Eq. (24) is marched through time using the forward difference algorithm [Hughes 2000] to give

$$\tilde{\theta}_{n+1} = \tilde{\theta}_n + \Delta t \dot{\tilde{\theta}}_n \quad (40)$$

$$\mathbf{C}^l \dot{\tilde{\theta}}_n + \mathbf{H}_n \tilde{\theta}_n = \mathbf{P}_n \quad (41)$$

It is also suffices to integrate the mechanical equation (25) by the central difference integration algorithm to yield

$$\dot{\tilde{\mathbf{U}}}_{n+1/2} = \dot{\tilde{\mathbf{U}}}_{n-1/2} + \frac{\Delta t_{n+1} + \Delta t_n}{2} \ddot{\tilde{\mathbf{U}}}_n \quad (42)$$

$$\dot{\tilde{\mathbf{U}}}_{n+1} = \dot{\tilde{\mathbf{U}}}_n + \Delta t_{n+1} \ddot{\tilde{\mathbf{U}}}_{n+1/2} \quad (43)$$

$$\mathbf{M}^l \ddot{\tilde{\mathbf{U}}}_n = \mathbf{F}_n^{ext} + \mathbf{F}_n^c - \mathbf{F}_n^{int} \quad (44)$$

where the capacity matrix  $\mathbf{C}$  and mass matrix  $\mathbf{M}$  are advantageously replaced by the lumped matrices  $\mathbf{C}^l$  and  $\mathbf{M}^l$  in thermal and mechanical equations respectively in the explicit analysis. Using the Lagrangian meshfree shape functions, the position vector for integration point is updated by

$$\mathbf{x}_g(\mathbf{X}, t_{n+1}) = \sum_{I=1}^{NP} \Psi_I(\mathbf{X}_g) \tilde{\mathbf{x}}_I(\mathbf{X}, t_{n+1}) \quad (45)$$

where the integration point position  $\mathbf{X}_g$  is initially located at the centroid of the integration cell and moves with material flow to its current position  $\mathbf{x}_g(\mathbf{X}, t_{n+1})$ . In contrast to the finite element method, the current position of integration point  $\mathbf{x}_g$  need not reside in the integration cell. Following the notation in Eq. (23),  $\tilde{\mathbf{x}}_I(\mathbf{X}, t_{n+1}) := \mathbf{X}_I + \tilde{\mathbf{u}}_I(\mathbf{X}, t_{n+1})$  is defined to be the “generalized” current position of node  $I$ . Subsequently, the deformation gradient at  $t=t_{n+1}$  is computed using Eqs. (34) and (45) to give

$$\begin{aligned} F_{ij}(\mathbf{x}_g(\mathbf{X}, t_{n+1})) &= \sum_{I=1}^{NP} \frac{\partial \Psi_I(\mathbf{X}_g)}{\partial X_j} \tilde{x}_{iI}(\mathbf{X}, t_{n+1}) \\ &= \sum_{I=1}^{NP} \frac{\partial \Psi_I(\mathbf{X}_g)}{\partial X_j} (X_{iI} + \tilde{u}_{iI}(\mathbf{X}, t_{n+1})) = \delta_{ij} + \sum_{I=1}^{NP} \frac{\partial \Psi_I(\mathbf{X}_g)}{\partial X_j} \tilde{u}_{iI}(\mathbf{X}, t_{n+1}) \end{aligned} \quad (46)$$

For the computational efficiency in explicit time integration method, the material derivatives of meshfree shape functions are always computed and stored at the first Lagrangian time step and reuse them during the time stepping.

In the staggered time-stepping scheme, the thermo-mechanical system is partitioned into two phases, the isothermal mechanical phase and the rigid conduction phase, during each time increment. The isothermal mechanical phase assumes a constant temperature during the mechanical computation and the rigid conduction phase considers the constant heat generation in the thermal computation at fixed configuration. A numerical stability requirement limits the maximum time increment in the explicit method for each phase. The overall stable time increment is then defined as the smaller of the two phases. In practice, the mechanical equations always set the critical time step for stability due to much smaller time scale associated with the mechanical problem.

### 3. Two-way Adaptive Procedure and Remap Algorithm

As mentioned earlier in the introduction, the major difficulty arises from the numerical modeling of FSW process when it comes to large deformation simulation of the complex material flow in frictional heating and stirring motion. Strictly Lagrangian approach based on a fix mesh in finite element method experiences difficulty in dealing with mesh entanglement due to unconstrained material flows. Although the meshfree Galerkin method using Lagrangian kernel helps improve the mesh entanglement problem in finite element method, it is prohibitively extending the range of meshfree applicability to model severe deformation that goes beyond the Lagrangian description [Rabcuzk 2004], i.e, the discretized deformation mapping ceases to be injective:

$$J_0 = \det(\mathbf{F}(\mathbf{x}_g(\mathbf{X}, t_n))) < 0 \quad (47)$$

One way to sidestep this numerical difficulty is to consider the semi-Lagrangian kernel [Guan 2011] used for the Reproducing Kernel Particle method [Liu 1995; Chen 1996] in impact and penetration simulation. The advantage of semi-Lagrangian kernel approach lies in its ability to reorder the neighboring nodal information such that a reconstruction of the Lagrangian meshfree shape functions is allowed and the possibility of non-positive Jacobin determinant in Eq. (47) is suppressed. Another way to evade the non-positive Jacobin determinant problem is to adopt an adaptive procedure similar to the combined rh-adaptive remeshing or global remeshing techniques in the finite element method. When compared with the semi-Lagrangian kernel approach, the adaptive method is able to refine the nodal density and generate accurate free surfaces for a better simulation in manufacturing problems. In this study, the adaptive method based on the concept of global remeshing is adopted and an anisotropic unstructured tetrahedral mesh is pursued to model the complex geometries evolved in the formation of stirring zone. A set of meshfree nodes is extracted from the unstructured tetrahedral mesh created by a mesh generator and used for the reconstruction of the Lagrangian meshfree shape functions. The set of contact boundary nodes can also be obtained from the generated tetrahedral mesh. While most research in adaptive error estimation has focused on the development of an accurate error estimator on linear analysis, formidable difficulties still remain in nonlinear analysis. For example, the well-known Z-Z error [Zienkiewicz 1987] developed based on super-convergence properties for linear problems cannot quantitatively be estimated in nonlinear problem. Therefore Z-Z error estimator can only be considered as an error indicator in nonlinear problems. In engineering practice the use of an efficient error indicator turns out to be more desirable particularly in the explicit time integration method. In this study, a point-wise error indicator based on the shear deformation is used to trigger the adaptive procedure for the von Mises

material. The global mesh generation in this study is comprised of an anisotropic surface Delaunay triangulation [George 1998] and an Advancing Front tetrahedral mesh generation [Lohner 1988]. An adaptive solution is then completed by mapping the solution variables between the old and new spatial discretization. Apparently, the element or patch-based remap procedures [Bucher 2007] are not suitable for the meshfree method. In this study, we introduce a second-order accurate projection operation based on the meshfree convex approximation [Wu 2011] to transfer the solution variables. If the global remesher fails to decompose the computation domain into tetrahedrons, an alternative meshfree adaptive procedure is taken to reconstruct the neighboring nodal information using the old discretization. A sketch of the two-way adaptive procedure is illustrated in Fig. 1.

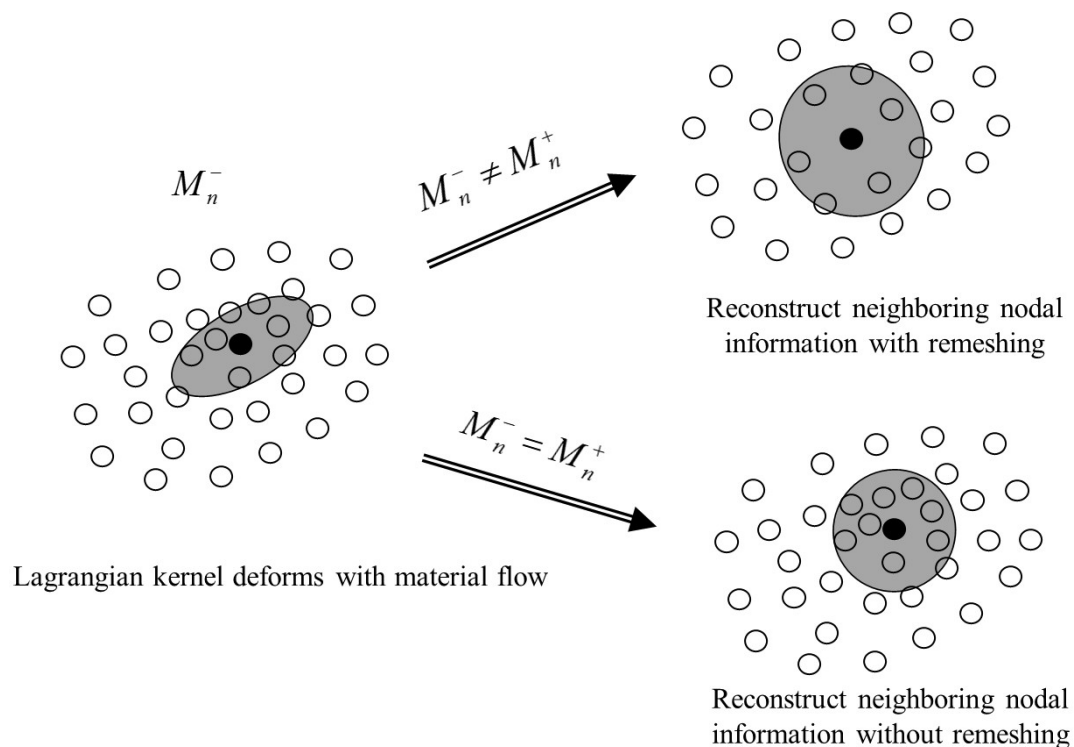


Figure 1. A sketch of the two-way adaptive procedure in two-dimensional case.

The basic steps in an adaptive solution strategy are summarized as below.

- (a) Compute the initial solution.
- (b) Estimate the point-wise error indicator in solution and interactively trigger the mesh generator as error indicated.
- (c) Input the deformed mesh at the beginning of each adaptive step and use it to define the surface domain.
- (d) Approximate the surface domain by a generalized Farin's algorithm [Farin 1986].
- (e) Perform the anisotropic surface triangulation based on a metric map with Delaunay kernel [George 1998] and yield the initial front of triangular faces. If there are any non-Delaunay facets in the constraining surfaces, insertion of Steiner points [Moller 1995] will be made and surfaces edges and faces will be recovered by a series of swaps or flips. In this study we exclusively consider the non-intersecting facets are triangle.

- (f) Conduct the Advancing Front method which consists of filling the empty space defined by the initial front and creating tetrahedrons one at a time and updating the front with created faces. A quadtree data structure [Samet 1990] is utilized for the proximity search and insertion or deletion of the front points.
- (g) Reconstruct the neighboring nodal information using the old discretization if any step in (d)~(f) fails. Go to step (i).
- (h) Perform the projection operation, transfer the solution valuables and update all nodal and internal valuables.
- (i) Initialize the solution and construct the approximations based on the new nodal distribution using the Lagrangian meshfree shape functions.
- (j) Resume the numerical solution procedure.

A customized point-wise error indicator  $\mathcal{G}$  introduced in step (b) is based on a shear deformation measure and is computed from the deformation gradient in Eq. (33). This error indicator is defined by

$$\mathcal{G}: Y_l^t \rightarrow [0, \infty), \mathcal{G} = 0.5 \cdot \max_g \left\{ \sum_{i,j}^3 |F_{ij}(\mathbf{x}_g(\mathbf{X}, t_n))| \right\}, i \neq j, \mathbf{x}_g \in Y_l^t \quad (48)$$

where  $Y_l^t$  denotes the collection of integration points at time  $t=t_n$ . The value 0.5 in Eq. (48) is made in average-sense since the deformation gradient is generally not symmetric. When the point-wise error indicator exceeds an acceptable level, the adaptive procedure is triggered to create a new discretization in the deformed configuration. The implementation details of the anisotropic surface Delaunay triangulation and the Advancing Front tetrahedral mesh generation can be found elsewhere [George 1998; Lohner 1988] and therefore is omitted in this paper. After a new mesh is generated, the remap procedure is performed to transfer the solution valuables from the old spatial discretization to the new spatial discretization. We denote the variables before and after the each remap to be superscripted with “-“ and “+”, respectively. Subsequently, we denote the unstructured tetrahedral meshes before and after remap at time  $= t_n$  by  $M_n^-$  and  $M_n^+$ . For nodal value  $z_l^+$  its remap is defined by the following projection operation

$$z_l^+(\mathbf{X}_l^+) = \sum_{J=1}^{NP^-} \Phi_J^-(\mathbf{X}_l^+) \tilde{z}_J^-(\mathbf{X}_J^-) \quad \forall \mathbf{X}_l^+ \in M_n^+ \quad (49)$$

From the definition in Eq. (22), we have

$$z_k^-(\mathbf{X}_k^-) = \sum_{J=1}^{NP^-} \Phi_J^-(\mathbf{X}_k^-) \tilde{z}_J^-(\mathbf{X}_J^-) \quad \forall \mathbf{X}_k^- \in M_n^- \quad (50)$$

or equivalently

$$\tilde{z}_J^-(\mathbf{X}_J^-) = \sum_{K=1}^{NP^-} (A_{JK}^-)^{-T} z_K^-(\mathbf{X}_K^-) \quad (51)$$

where  $A_{JK}^- = \Phi_J^-(\mathbf{X}_K^-)$ . Substituting Eq. (51) into (49) yields

$$\begin{aligned}
z_l^+(\mathbf{X}_l^+) &= \sum_{J=1}^{NP^-} \Phi_J^-(\mathbf{X}_l^+) \tilde{z}_J^-(\mathbf{X}_J^-) = \sum_{J=1}^{NP^-} \sum_{K=1}^{NP^-} \Phi_J^-(\mathbf{X}_l^+) (A_{JK}^-)^{-T} z_K^-(\mathbf{X}_K^-) \\
&= \sum_{K=1}^{NP^-} \bar{\Phi}_K^-(\mathbf{X}_l^+) z_K^-(\mathbf{X}_K^-) \quad \forall \mathbf{X}_l^+ \in M_n^+
\end{aligned} \tag{52}$$

where

$$\bar{\Phi}_K^-(\mathbf{X}_l^+) = \sum_{J=1}^{NP^-} (A_{KJ}^-)^{-1} \Phi_J^-(\mathbf{X}_l^+) \tag{53}$$

$\bar{\Phi}_K^-$  in Eq. (52) is the remap function which satisfies the following interpolation property

$$\bar{\Phi}_K^-(\mathbf{X}_l^-) = \sum_{J=1}^{NP^-} (A_{KJ}^-)^{-1} \Phi_J^-(\mathbf{X}_l^-) = \sum_{J=1}^{NP^-} (A_{KJ}^-)^{-1} A_{Jl}^- = \delta_{Kl} \tag{54}$$

as well as the following linear polynomial reproduction property

$$\begin{aligned}
\sum_{K=1}^{NP^-} \bar{\Phi}_K^-(\mathbf{X}) \mathbf{X}_K^- &= \sum_{K=1}^{NP^-} \sum_{J=1}^{NP^-} (A_{KJ}^-)^{-1} \Phi_J^-(\mathbf{X}) \mathbf{X}_K^- \\
&= \sum_{J=1}^{NP^-} \sum_{K=1}^{NP^-} (A_{KJ}^-)^{-1} \mathbf{X}_K^- \Phi_J^-(\mathbf{X}) = \sum_{J=1}^{NP^-} \mathbf{X}_J^- \Phi_J^-(\mathbf{X}) = \mathbf{X} \quad \forall \mathbf{X} \in M_n^-
\end{aligned} \tag{55}$$

Since the remap algorithm preserves linearly-varying nodal values, it is second-order accurate in space. In each remap procedure,  $\Phi_J^-$ ,  $J=1, \dots, NP^-$  are the newly constructed meshfree shape functions evaluated on the current configuration based on the old spatial discretization  $M_n^-$ . The tilde symbol in Eq. (49) stands for a “generalized” nodal quantity as defined in Eq. (22). If any boundary node  $\mathbf{X}_l^+$  does not reside on the old spatial discretization  $M_n^-$ , an appropriate projection is performed to find the closest point on the boundary of  $M_n^-$  for the subsequent remapping. We proceed to show that the above remap procedure is consistent in the sense that if the new discretization is identical to the old discretization, then all nodal quantities will remain unchanged after the remap.

$$\begin{aligned}
z_l^+(\mathbf{X}_l^+) &= \sum_{J=1}^{NP^-} \Phi_J^-(\mathbf{X}_l^+) \tilde{z}_J^-(\mathbf{X}_J^-) \\
&= \sum_{J=1}^{NP^-} \bar{\Phi}_J^-(\mathbf{X}_l^+) z_J^-(\mathbf{X}_J^-) \\
&= \sum_{J=1}^{NP^-} \bar{\Phi}_J^-(\mathbf{X}_l^-) z_J^-(\mathbf{X}_J^-) \\
&= \sum_{J=1}^{NP^-} \delta_{lJ} z_J^-(\mathbf{X}_J^-) = z_l^-(\mathbf{X}_l^-) \quad \forall \mathbf{X}_l^+ = \mathbf{X}_l^-, M_n^+ = M_n^-
\end{aligned} \tag{56}$$

Similarly, another consistent remap procedure is performed for the state valuable  $s_g$  such as effective plastic strain, stress components and other internal valuables sampled at the integration point per integration cell.

$$\begin{aligned} s_g^+(\mathbf{X}_g^+) &= \sum_{j=1}^{mp^-} \phi_j^-(\mathbf{X}_g^+) \tilde{s}_j^-(\mathbf{X}_j^-) = \sum_{j=1}^{mp^-} \sum_{k=1}^{mp^-} \phi_j^-(\mathbf{X}_g^+) (B_{jk}^-)^{-T} s_k^-(\mathbf{X}_k^-) \\ &= \sum_{k=1}^{mp^-} \bar{\phi}_k^-(\mathbf{X}_g^+) s_k^-(\mathbf{X}_k^-) \quad \forall \mathbf{X}_g^+ \in M_n^+ \end{aligned} \quad (57)$$

where

$$\bar{\phi}_k^-(\mathbf{X}_g^+) = \sum_{j=1}^{mp^-} B_{kj}^{-1} \phi_j^-(\mathbf{X}_g^+) \quad (58)$$

The matrices  $B_{jk}^- = \phi_j^-(\mathbf{X}_k^-)$  are computed on the set of integration points defined on the current configuration using the GMF method. The summation “ $mp^-$ ” denotes the total number of integration points in the old discretization. It is known that the Advancing Front technique usually encounters difficulty when fronts merge. As a result, highly distorted tetrahedrons can occur in the generated mesh and greatly affects the accuracy of finite element solution. Since the construction of Lagrangian meshfree shape functions in this study does not rely on the finite element mesh, a distinct advantage of the proposed method in the adaptive procedure is its insensitivity to the existence of highly distorted tetrahedrons in the mesh.

A noteworthy addition to the proposed method is its flexibility in reconstructing the neighboring nodal information without remeshing. In conventional finite element analysis, when the global remesher is unable to generate the desired discretization at time  $t=t_n$  under certain geometrical conditions, the adaptive procedure is aborted and causes termination in the simulation. With the current method, the second way for adaptive procedure will step in and replaces the global remeshing step. Under this scenario, a meshfree nodal reconstruction step is taken which maintains the material quantities for all nodal and integration points in the Lagrangian setting but requires a new neighbor search. Using the chain rule, the calculation for the deformation gradient becomes

$$\mathbf{F}_{n+1} = \bar{\mathbf{F}}_{n+1} \mathbf{F}_n \quad (59)$$

where  $\bar{\mathbf{F}}_{n+1}$  is the decomposed deformation gradient due to the reconstruction of meshfree shape functions  $\bar{\Psi}_l$  and is given by

$$\bar{\mathbf{F}}_{n+1,ij}(\mathbf{x}_g) = \sum_{l=1}^{NP} \frac{\partial \bar{\Psi}_l(\bar{\mathbf{x}}_g)}{\partial \bar{\mathbf{x}}_j} \tilde{x}_{il}(\bar{\mathbf{x}}, t_{n+1}) \quad \forall \bar{\mathbf{x}} \in \Omega_{\bar{\mathbf{x}}} \quad (60)$$

$$\tilde{x}_l(\bar{\mathbf{x}}, t_{n+1}) = \mathbf{x}_l(\mathbf{X}, t_n) + \tilde{\mathbf{u}}_l(\bar{\mathbf{x}}, t_{n+1}) = \bar{\mathbf{x}}_l + \tilde{\mathbf{u}}_l(\bar{\mathbf{x}}, t_{n+1}) \quad (61)$$

Here, we define  $\bar{\mathbf{x}} = \mathbf{x}(\mathbf{X}, t_n)$  to be a position vector on a new reference configuration  $\Omega_{\bar{\mathbf{x}}}$  at time  $t=t_n$ . Since this meshfree nodal reconstruction step does not involve remeshing, the remap

procedures are not needed. The updated deformation gradients together with the reconstructed shape functions and their derivatives are used to evaluate the discrete terms in Section 3.1. This flexibility in choosing different adaptive procedures provides an incentive for the use of adaptive meshfree Galerkin method in large deformation analysis of manufacturing problems.

## 6. Numerical Simulation

In this section, we consider a FSW problem as shown in Fig. 2. The light blue part is the tool, and the dark blue one is the work piece. The green part is rigid to provide the global constraints. The detail dimensions are shown in Fig. 3. The initial mesh of work piece is plotted in Fig. 4, which is going to be locally refined with respect to the contact surface curvature of the tool.

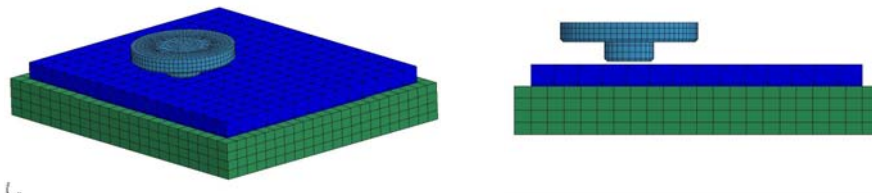


Figure 2. FSW simulation model

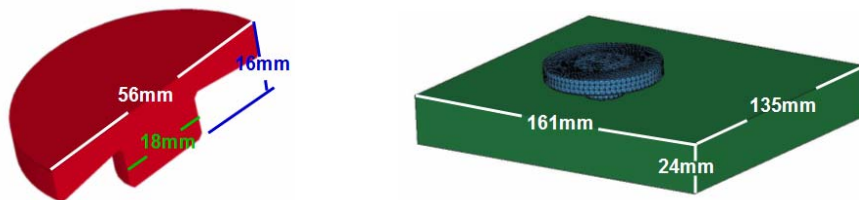


Figure 3. Dimensions of the tool and work piece

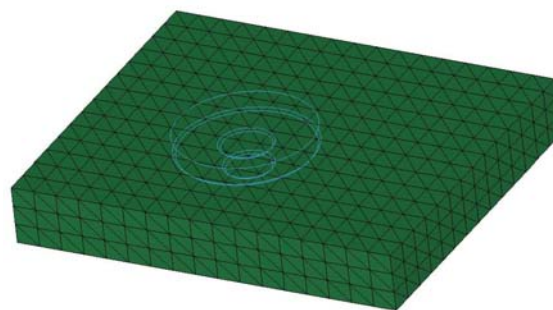


Figure 4. Initial mesh of the work piece

The tool has a conical shoulder surface to shape the material pushed out by two sequential stages of the FSW process:

- (1) Plunge stage: the rotating tool plunges into the work piece along vertical direction;
- (2) Traverse stage: the rotating tool travels along horizontal direction.

The material model of the work piece is assumed to be temperature dependant ideal plasticity. The material parameters are reported in table 1. The temperature dependant yield stresses of the work piece are listed in table 2. The melting point of work material is around  $1080^{\circ}C$ .

Table 1. Material parameters

	Density ( $kg \cdot m^{-3}$ )	Thermal (Isotropic) Heat capacity ( $J \cdot kg^{-1} \cdot ^{\circ}C$ )	Thermal conductivity ( $W \cdot m^{-1} \cdot K^{-1}$ )	Young's Modulus ( $GPa$ )	Poisson's ratio
Tool	7850	434	60	<i>rigid</i>	
Work piece	2700	875	175	70	0.3

Table 2. Yield stresses of the work piece

Temperature ( $^{\circ}C$ )	20	100	300	550	800	1080
$\sigma_y$ (MPa)	324	300	253	196	131	70

The tool has a constant rotating speed  $125 \text{ rad} \cdot \text{s}^{-1}$ . The plunge displacement curve and traverse speed curve can be found in Fig. 5.

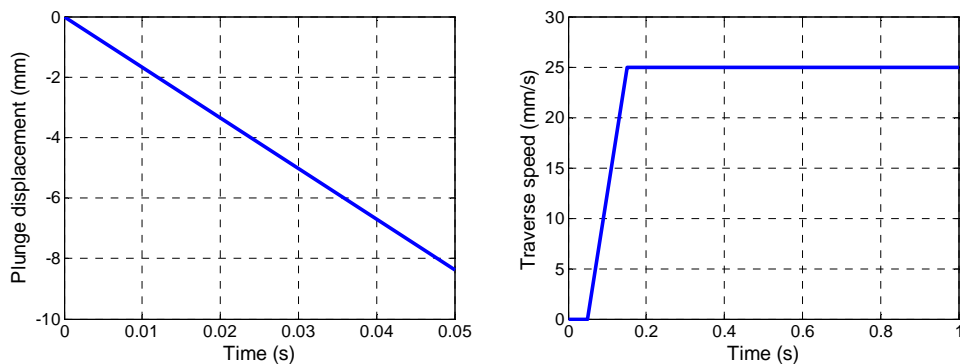
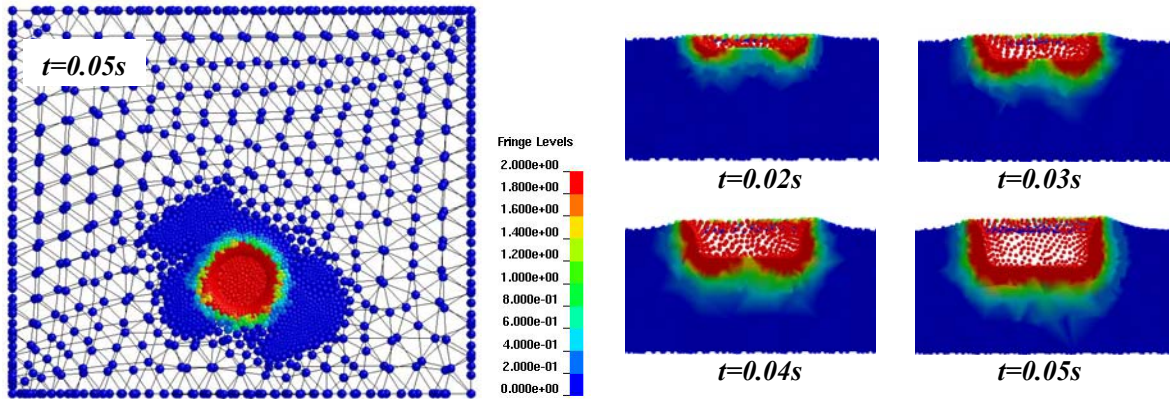


Figure 5. Plunge displacement and traverse speed curve of the tool

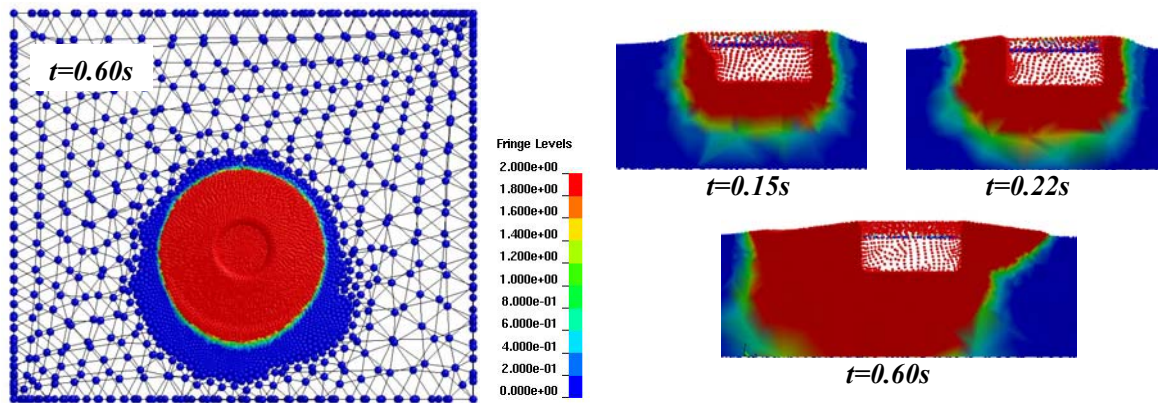
The thermal mortar contact is defined between the tool and work piece with the Coulomb's frictional coefficient 0.7. A constant temperature  $20^{\circ}C$  is applied to all the parts as initial condition.

The normalized support size of the meshfree GMF approximation is 1.1. Since the density of nodal distribution varies dramatically throughout the domain due to local refinement, the actual nodal support size for every node is adjusted according to its surrounding nodal distribution to improve overall computational performance. The pressure smoothing scheme [Hu 2010] is applied to improve the smoothness and accuracy of stress calculation. By using local adaptivity, the integration cell size varies between  $1\text{mm}$  and  $8\text{mm}$ . The maximum time step is  $0.5\text{ms}$ . The total processing time in this study is 1s.

The analysis was done by MPP double precision LS-DYNA with 4 Xeon E5520 cores. The total computational time was about 17 hours. There were around 400 adaptive steps that gradually increased the number of integration cells from ~4,000 to ~130,000.



(a) Plunge stage



(b) Traverse stage

Figure 6. Plastic deformation contour plots

Figure 6 plots the deformation in two stages, where the top view is to the left and the central cross-section view is to the right. The material flow and free surface are well captured and represented by the local adaptive re-meshing. The red zone with large effective plastic strain clearly shows the stirring region during the welding process. Figure 7 shows the temperature results of both work piece and tool at three different processing steps. The model is plotted by cutting through the central cross-section to better provide the temperature distribution inside the parts. At the end of plunge stage at  $t=0.05s$ , the maximum temperature is around the front edge of the tool contact surface where the most heat sources from frictional contact are generated. In the traverse stage at  $t=0.60s$ , there is a “V” shape contour due to high gradient temperature distribution in the stirring zone, and the maximum temperature is close to the melting point. Figure 8 gives the von Mises stress results, where material softening can be clearly observed as the temperature increases from the plunge stage to traverse stage. The energy curve of the work piece and the tool contact force curve are plotted in Fig. 9.

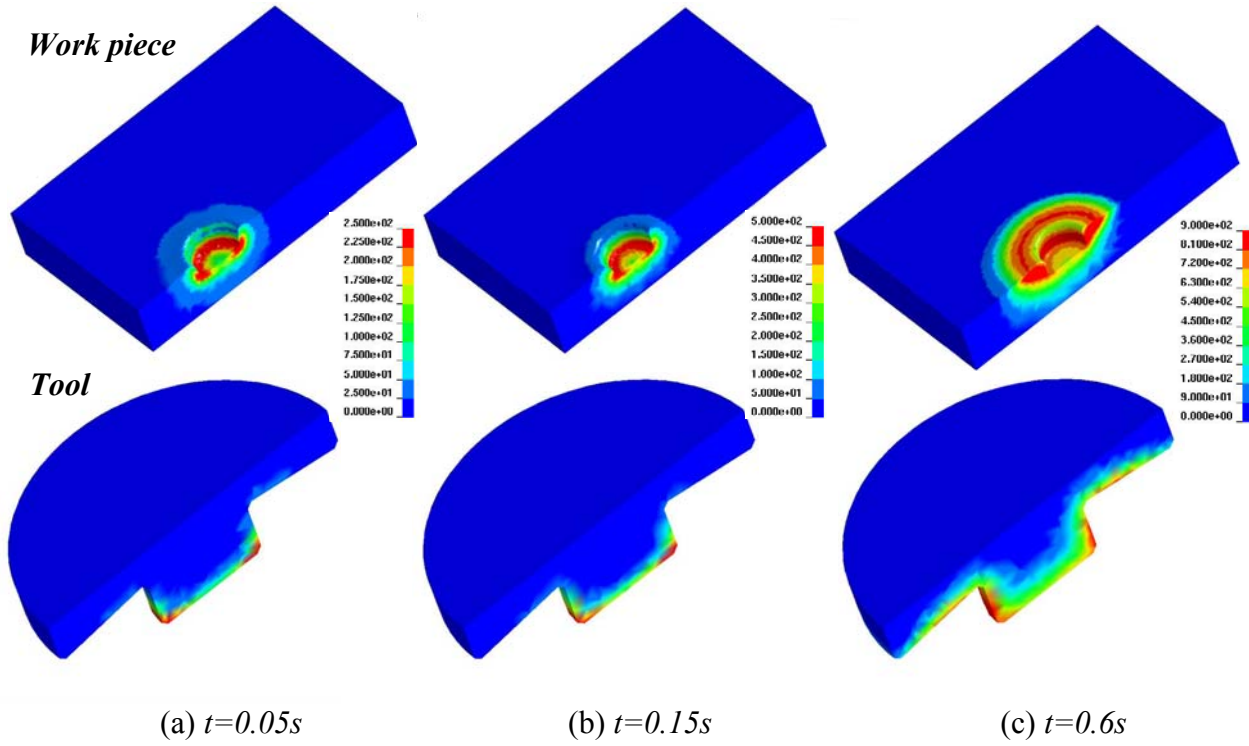


Figure 7. Temperature contour plots

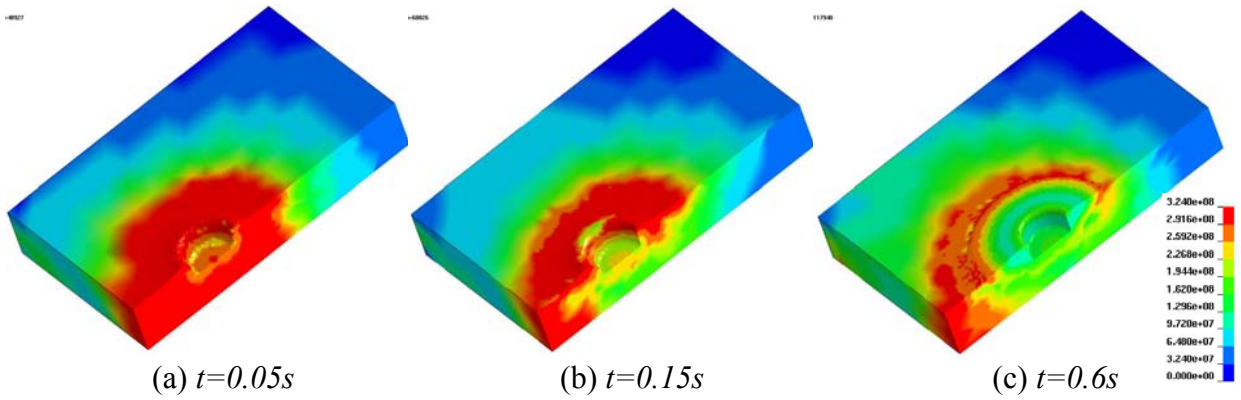


Figure 8. von Mises stress contour plots

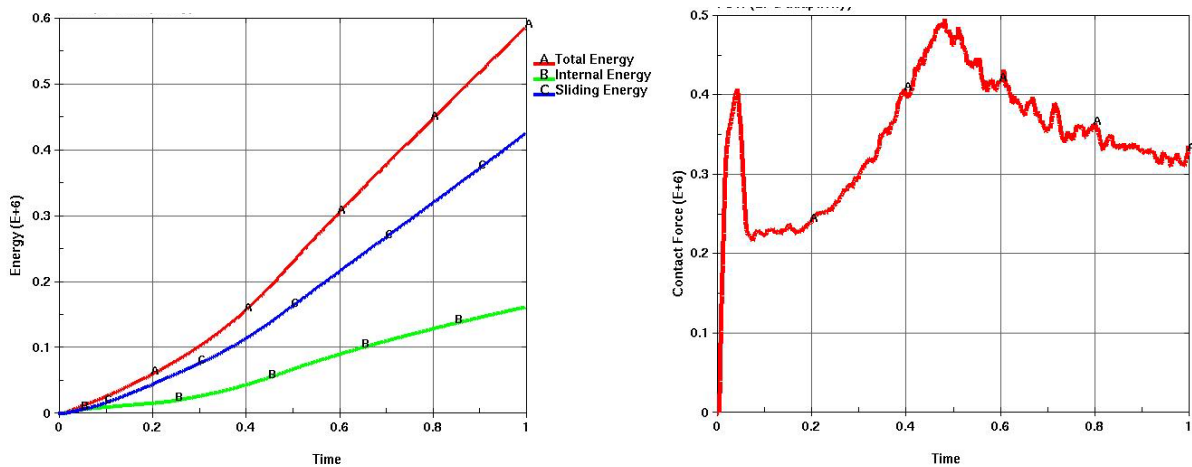


Figure 9. Energy curve of work piece and tool contact force curve

## Conclusion

The thermo-mechanical complexity and severe material flow of friction stir welding process make analytical models incapable of capturing all the details needed for the satisfactory quantitative prediction of temperature and stress fields generated in the work piece. Via numerical modeling techniques, various finite element models of the friction stir welding process have been developed to help visualize and study the fundamental thermo-mechanical behavior of work piece and input parameters of the tool. However, there still exist great numerical challenges for the finite element simulation of friction stir welding process when the issues of handling severe mesh distortion, modeling contact and traction-free boundary conditions, imposing volume-constraint, performing accurate state variable remap and maintaining the quality of adaptive mesh are simultaneously presented in the model. This paper attempts to provide an alternative approach using a two-way adaptive meshfree Galerkin method to overcome those numerical challenges.

In our approach, the coupled thermo-mechanical equations using a staggered explicit time integration scheme are modeled within a Lagrangian framework. This approach facilitates a direct incorporation of the displacement-based meshfree formulation with the adaptive procedures to circumvent the severe mesh distortion and volume-constraint problems. The concept of the two-way adaptive procedure is introduced to bypass the numerical difficulty caused by the abortion of adaptive mesh generation. Lagrangian meshfree convex approximation plays a key role in simplifying the boundary condition enforcement, suppressing tensile instability, minimizing the adaptivity-induced discretization sensitivity and offering an accurate and consistent projection operation in the remap procedure. The proposed method meets all the computational requirements suggested by Neto [Neto 2013] for FSW analysis including (1) Consideration of rotational boundary condition; (2) Consideration frictional contact; (3) Support for very high levels of deformation; (4) Support for elastic-plastic or elastic-viscoplastic material models; and (5) Support for complex geometry.

## Acknowledgements

The authors wish to thank Dr. John O. Hallquist of LSTC for his support to this research. The authors would also like to thank Dr. Art Shapiro for the technical discussions.

## References

1. Bucher, A., Meyer, A., Görke, U. J. and Kreißig, R. (2007), "A comparison of mapping algorithms for hierarchical adaptive FEM in finite elasto-plasticity", *Computational Mechanics*, **39**, 521-536.
2. Chen, J. S., Pan, C., Wu, C. T. and Liu, W. K. (1996), "Reproducing kernel particle methods for large deformation analysis of non-linear structures", *Comput. Meth. Appl. Mech. Eng.*, **139**, 195-227.
3. Dawes C. J. and Thomas, W. M. (1996), "Friction stir process welds in aluminum alloys", *Welding Journal*, **75**(3), 41-45.
4. Farin, G. (1986), "Triangular Bernstein-Bezier patches", *Computer Aided Geometric Design*,

- 3(2), 83-128.
5. George, P. and Borouchaki, H., Delaunay triangulation and meshing: application to finite elements. Hermes, Paris, 1998.
  6. Guan, P. C., Chi, S. W., Chen, J. S., Slawson, T. R., and Roth, M. J. (2011), "Semi-Lagrangian reproducing kernel particle method for fragment-impact problems", *International Journal of Impact Engineering*, **38**(12), 1033-1047.
  7. Hughes, T. J. R., The Finite Element Method. Prentice-hall, Englewood Cliffs, NJ, 2000.
  8. Hu, S., Wu, C. T. and Guo, Y. (2010), "Engine Impeller Sub-Fragmentation Simulation Using EFG Method", *11th International LS-DYNA Users Conference, Aerospace(1)*, 1-27.
  9. Hu, W., Wu, C. T. and Saito, K. (2010), "Meshfree Interactive Adaptivity and Its Application", *11th International LS-DYNA Users Conference, Metal forming*, 10-21.
  10. Koric, S., Hibbeler, L. C. and Thomas. B. G. (2009), "Explicit coupled thermo-mechanical finite element model of steel solidification", *Int. J. Numer. Meth. Engrg.*, **78**, 1-31.
  11. Liu, W.K., Jun, S. and Zhang, Y.F. (1995), "Reproducing kernel particle methods", *Int. J. Numer. Meth. Fluids*, **20**, 1081-1106.
  12. Lohner, R. and Parikh, P. (1988), "Generation of three-dimensional unstructured grids by the advanced-front method", *Int. J. Numer. Meth. Fluids*, **8**, 1035-1149.
  13. Lorrain, O., Serri, J., Favier, V, Zahrouni, H. and El Hadrouz, M. (2009), "A contribution to a critical review of friction stir welding numerical simulation", *Journal of Mechanics of Materials and Structures*, **4**(2), 351-369.
  14. Lu, H. and Wu, C. T. (2006), "A grid-based adaptive scheme for the three-dimensional forging and extrusion problems with the EFG method", *9th International LS-DYNA Users Conference*, **17**, 33-44.
  15. Lu, H. S., Wu, C. T. and Xu, J. X. (2008), "Forging and extrusion analysis with LS-DYNA using 3D adaptive EFG method", *10th International LS-DYNA Users Conference*, **17**, 21-24.
  16. Marusich, T. D., Ortiz, M. (1995), "Modeling and simulation of high-speed machining", *International Journal for Numerical Methods in Engineering*, **38**, 3675-3694.
  17. Moller, P, and Hansbo, P. (1995), "On advancing front mesh generation in three dimensions", *International Journal for Numerical Methods in Engineering*, **38**, 3551-3569.
  18. Neto, D. M. and Neto P. (2013), "Numerical modeling of friction stir welding process: a literature review", *Int. J. Adv. Manuf. Technol.*, **65**, 115-126.
  19. Pashazadeh, H., Masoumi, A. and Teimournezhad, J. (2013), "A 3D numerical model to investigate mechanical, thermal and material flow characteristics in friction stir welding of copper sheets", *Int. J. Auto. Engrg.*, **3**(1), 328-342.
  20. Puso, M., Chen, J. S., Zywick, E, and Elmer, W. (2008), "Meshfree and finite element nodal integration methods", *International Journal for Numerical Methods in Engineering*, **74**, 416-446.
  21. Rabczuk, T., Belystchko, T. and Xiao, S. P. (2004), "Stable particle methods based on Lagrangian kernels", *Comp. Meth. Appl. Mech. Eng.*, **193**, 1035-1063.
  22. Samet, H. The Design and Analysis of Spatial Data Structures. Addison-Wesley, Reading, 1990.
  23. Sukumar N. (2004), "Construction of polygonal interpolants: a maximum entropy approach", *International Journal for Numerical Methods in Engineering*, **61**, 2159-2181.
  24. Wang, H. P., Wu, C. T., Guo, Y. and Botkin, M. (2009), "A Coupled Meshfree/finite Element Method for Automotive Crashworthiness Simulations," *International Journal of Impact Engineering*, **36**, 1210-1222.
  25. Wu, C. T., Chen, J. S., Chi, L and Huck, F. (2001), "A Lagrangian meshfree formulation for analysis of geotechnical materials," *Journal of Engineering Mechanics*, **127**, 440-449.

26. Wu, C. T. and Lu, H. S. (2009), "Practical fast meshfree analysis", U.S. Patent.
27. Wu, C.T., Park, C.K. and Chen, J.S. (2011), "A generalized approximation for the meshfree analysis of solids", *Int. J. Numer. Meth. Engrg.*, **85**, 693-722.
28. Wu, C.T., Hu, W., Wang, H.P. and Lu, H. (2014), "An adaptive meshfree Galerkin method for the three-dimensional thermo-mechanical flow simulation of friction stir welding process", *J. Comp. Phys.* (to be submitted)
29. Zienkiewicz, O. C. and Zhu, J. Z. (1987), "A simple error estimator and adaptive procedure for practical engineering analysis, *Int. J. Numer. Meth. Engrg.*, **24**, 337-357.

